



# Fire-extinguishing, recyclable liquefied gas electrolytes for temperature-resilient lithium-metal batteries

Yijie Yin<sup>1,6</sup>, Yangyuchen Yang<sup>1,6</sup>✉, Diyi Cheng<sup>1</sup>, Matthew Mayer<sup>2</sup>, John Holoubek<sup>1,2</sup>, Weikang Li<sup>2</sup>, Ganesh Raghavendran<sup>1,2</sup>, Alex Liu<sup>2</sup>, Bingyu Lu<sup>2</sup>, Daniel M. Davies<sup>2</sup>, Zheng Chen<sup>1,2,3</sup>, Oleg Borodin<sup>1,4</sup>✉ and Y. Shirley Meng<sup>1,2,3,5</sup>✉

**High-energy density, improved safety, temperature resilience and sustainability are desirable properties for lithium-battery electrolytes, yet these metrics are rarely achieved simultaneously. Inspired by the compositions of clean fire-extinguishing agents, we demonstrate inherently safe liquefied gas electrolytes based on 1,1,1,2-tetrafluoroethane and pentafluoroethane that maintain  $>3\text{ mS cm}^{-1}$  ionic conductivity from  $-78$  to  $+80\text{ }^{\circ}\text{C}$ . As a result of beneficial solvation chemistry and a fluorine-rich environment, lithium cycling at  $>99\%$  Coulombic efficiency for over 200 cycles at  $3\text{ mA cm}^{-2}$  and  $3\text{ mAh cm}^{-2}$  was demonstrated in addition to stable cycling of Li/NMC622 full batteries from  $-60$  to  $+55\text{ }^{\circ}\text{C}$ . In addition, we demonstrate a one-step solvent-recycling process based on the vapour pressure difference at different temperatures of the liquefied gas electrolytes, which promises sustainable operation at scale. This work provides a route to sustainable, temperature-resilient lithium-metal batteries with fire-extinguishing properties that maintain state-of-the-art electrochemical performance.**

In recent decades, the demand for high-energy secondary batteries has increased exponentially, with their applications expanding from portable electronics to electric vehicles and grid storage<sup>1</sup>. The lithium (Li) metal anode is considered as the most promising candidate for high-energy density rechargeable batteries due to its highest theoretical specific capacity ( $3,860\text{ mAh g}^{-1}$ ) and lowest electrochemical potential ( $-3.04\text{ V}$  versus the standard hydrogen electrode). However, safety concerns associated with dendrite growth, along with the limited cycle life and capacity decay at subzero temperature, have hampered their practical application. As the above issues are highly contingent on the physical and chemical properties of the battery electrolyte, the development of novel chemistries and design strategies is crucial to solving them.

To this end, a relatively limited number of battery electrolytes have demonstrated a highly reversible Li-metal performance that is capable of producing hundreds of cycles at the full-cell level<sup>2–4</sup>. Progress has been limited due to the parasitic reactions of Li metal with electrolytes from solid–electrolyte interphase (SEI) cracking, porous plating morphologies and dendrite formation, leading to the irreversibility of Li cycling<sup>5,6</sup>. Furthermore, atypical cycling temperatures introduce additional design complexity, where low temperatures have been demonstrated to result in dendritic morphologies and poor reversibility, and increased temperatures tend to exacerbate the parasitic reactivity of all kinds<sup>7</sup>. Even if these metrics were to be obtained in a single system, the inherent flammability of common solvents with desirable reductive stability (for example, ethers) is suboptimal<sup>3,8</sup>. Although non-flammable solvents exist, their long-term electrochemical stability is often problematic, caused mainly by their instability with the Li-metal anode<sup>9</sup>. To further

complicate these already stringent design considerations, the widespread production of Li-metal batteries is also highly dependent on the economic and environmental sustainability of the cells, where the recyclability of every component including the electrolyte is highly desirable<sup>10,11</sup>. Given all of these factors, the design of electrolyte systems that consist of temperature-resilient reversibility, inherently safe physical properties and a viable route to environmentally and economically sustainable application is a seemingly insurmountable challenge.

Extensive efforts have been devoted to developing non-flammable electrolytes, but all of them fail to satisfy the aforementioned requirements simultaneously. Solid-state electrolytes are regarded as promising candidates due to their non-flammable nature and high packing density that can potentially boost the energy density of batteries<sup>12</sup>. However, the ionic conductivity of solid-state electrolytes suffers even at moderately low temperatures ( $<0\text{ }^{\circ}\text{C}$ ), which casts doubt on their practical use where a wide temperature window is needed. Ionic-liquid electrolytes with molten salts present low volatility and low flammability (or even non-flammability); however, their high viscosity (particularly at low temperatures) and cost limit their applications<sup>13</sup>. Besides that, few to no reports of solid-state electrolytes or ionic liquids have demonstrated a viable Li-metal performance in full cells without the introduction of additional cell components<sup>14</sup>. In commonly used liquid electrolytes, organic non-flammable phosphate solvents such as trimethyl phosphate and triethyl phosphate have been explored to obtain enhanced safety<sup>15,16</sup>. Although such solvents are unable to produce stable SEI layers on either graphite or Li-metal anodes<sup>17,18</sup>, increasing the salt concentration of trimethyl phosphate-based electrolytes has been shown

<sup>1</sup>Materials Science and Engineering Program, University of California, San Diego, La Jolla, CA, USA. <sup>2</sup>Department of NanoEngineering, University of California, San Diego, La Jolla, CA, USA. <sup>3</sup>Sustainable Power and Energy Center, University of California, San Diego, La Jolla, CA, USA. <sup>4</sup>Battery Science Branch, US Army Combat Capabilities Development Command Army Research Laboratory, Adelphi, MD, USA. <sup>5</sup>Pritzker School of Molecular Engineering, University of Chicago, Chicago, IL, USA. <sup>6</sup>These authors contributed equally: Yijie Yin, Yangyuchen Yang. ✉e-mail: [yay081@eng.ucsd.edu](mailto:yay081@eng.ucsd.edu); [oleg.a.borodin.civ@army.mil](mailto:oleg.a.borodin.civ@army.mil); [shirleymeng@uchicago.edu](mailto:shirleymeng@uchicago.edu)

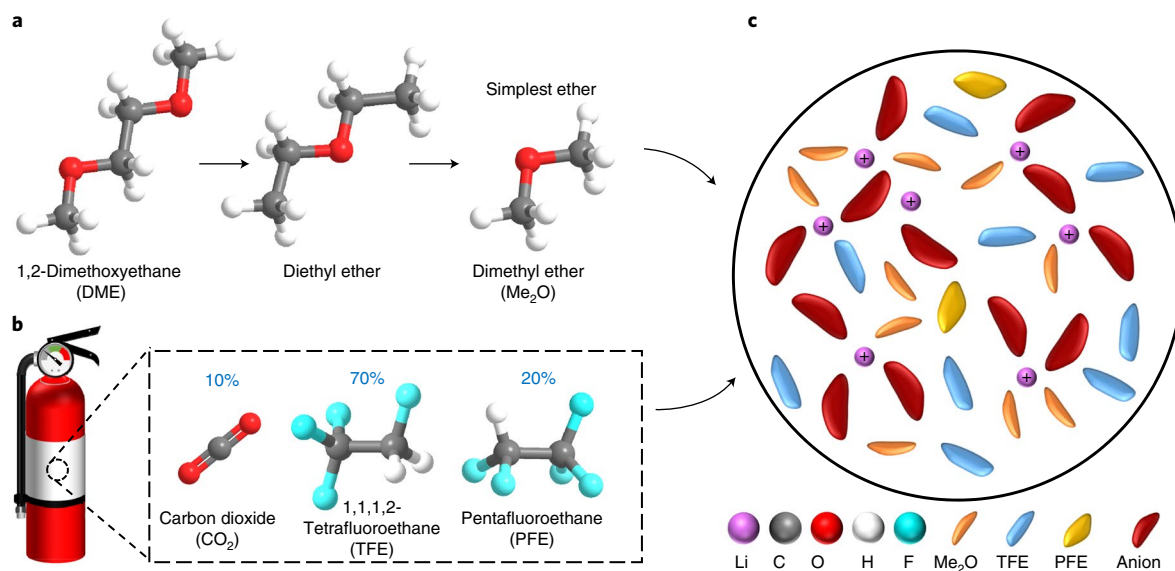


**Fig. 1 | Design of LGEs.** **a**, Selection of dimethyl ether, as the simplest ether with fast transport, strong Li<sup>+</sup> solvation and high salt solubility. **b**, Composition of the clean fire-suppressing agent FS 49 C2. **c**, Proposed solvation structure of the designed LGEs. Colours: Li<sup>+</sup>, purple; C, grey; O, red; H, white; F, cyan; Me<sub>2</sub>O, orange; TFE, blue; PFE, yellow; anion, maroon.

to promote salt-derived inorganic SEI layers and consequently improve the interface stability as well as maintain safe operation<sup>19</sup>. However, the cost, viscosity, electrode wetting and low-temperature performance are sacrificed in these high-concentration systems. More recently, localized high-concentration electrolytes (LHCEs) have been formulated by adding inert diluents to lower the viscosity of the whole electrolyte, improving upon the above-mentioned issues while maintaining all the desired properties for battery performance<sup>20,21</sup>. Based on this concept, non-flammable LHCEs were developed by coupling inert diluents like bis(2,2,2-trifluoroethyl) ether (BTFE) with non-flammable solvents such as trimethyl phosphate or triethyl phosphate<sup>22,23</sup>. Fire-retardant LHCEs have also been formulated using non-flammable diluents, for example 2,2,2-trifluoroethyl-1,1,2,2-tetrafluoroethyl ether (or HFE) with flammable solvents<sup>24</sup>. Although these LHCEs delivered a higher Coulombic efficiency (CE) for Li metal and better capacity retention over long-term cycling, the diluents are often flammable or decrease the conductivity of the electrolyte, with relatively low boiling points (BTFE, +62 °C; HFE, +57 °C) hindering their operation at higher temperature. Although the vast array of previously explored chemistries have made significant progress with improving either the electrochemical performance, safety or renewability metrics, an electrolyte chemistry that comprehensively addresses all of them has yet to be demonstrated<sup>25</sup>.

To circumvent the conventional liquid-phase temperature window, a transformative concept of using a variety of liquefied gas hydrofluorocarbons as the main solvents was proposed<sup>26</sup>. Owing to their ultralow viscosity and freezing point, these liquefied gas electrolytes (LGEs) display improved performance at low temperature. To expand on the original LGE systems, another advance in the performance was made through the addition of other co-solvents, such as tetrahydrofuran and acetonitrile, respectively, which resulted in stable Li plating and stripping over 500 cycles with an average CE of 99.6% and Li/NMC cycling with more than 96.5% capacity retention after 500 cycles<sup>27,28</sup>. However, the use of high-pressure and flammable gases cannot satisfy the previously discussed safety and environmental concerns.

Here, we report a versatile LGE for wide-temperature Li-metal batteries with intrinsic fire-extinguishing properties and economical recycling after utilization. Through the rational design

of electrolytes based on 1,1,1,2-tetrafluoroethane (TFE) and pentafluoroethane (PFE), we show a self-fire-extinguishing effect and demonstrate a simple one-step solvent-recycling process. Owing to a sufficiently high ionic conductivity over a wide temperature range, favourable solvation structure and SEI formation, the designed LGE showed stable Li-metal cycling with a CE of 99% and long-term Li/NMC622 cycling up to 4.2 V from -60 °C to +55 °C.

### Rational design of liquefied gas electrolytes

The desired liquefied gas solvents must satisfy a number of potentially conflicting criteria. Ideally, the liquefied gas solvent should possess a solvation ability sufficient for achieving >1 M salt solubility in addition to having a sufficiently low vapour pressure, low-/non-flammability, a low viscosity and a low freezing point. As no single solvent satisfies all criteria, we utilize a mixture of non-flammable, low-viscosity, low-vapour-pressure hydrofluorocarbons and Li<sup>+</sup> coordinating ethers to achieve a balanced electrolyte. Compared with the properties of different ethers (Fig. 1a), dimethyl ether (Me<sub>2</sub>O) exists in the gaseous state under ambient conditions. Of the ethers, it has the lowest freezing point and viscosity combined with a high solvating power, reductive stability and good compatibility with Li metal. By comparison with the previously reported fluoromethane solvent, Me<sub>2</sub>O has a higher critical point at 127 °C and a lower vapour pressure, that is, down to 75 psi at 20 °C (Table 1)<sup>29,30</sup>. Despite its flammability, Me<sub>2</sub>O generates non-toxic and non-corrosive products (for example, H<sub>2</sub>O) after combustion<sup>31</sup>, whereas the combustion of flammable fluorinated solvents such as fluoromethane and the more widely used BTFE results in the generation of hydrogen fluoride<sup>32</sup>.

To tackle the flammability issues, a non-flammable solvent needs to be the majority component in a mixture. The ideal non-flammable co-solvent would keep the aforementioned physical properties as well as a broad electrochemical window and a low solvation ability to maintain an ion-pairing solvation structure. Based on these principles and inspired by the fire-extinguishing agent FS 49 C2 (Fig. 1b; Supplementary Fig. 1, Supplementary Note 1), 1,1,1,2-tetrafluoroethane (TFE) and pentafluoroethane (PFE) were identified as potential liquefied gas co-solvents. With a high flash point (TFE,  $T_{\text{flash}} = 250$  °C), the non-flammability of PFE and high fluorine atomic ratios<sup>33,34</sup>, these molecules also exhibit a

**Table 1 | Physical properties of the different solvents**

| Solvent                          | Melting point (°C) | Boiling point (°C) | Critical point (°C) | Flash point (°C) | Vapour pressure (psi) | Dipole (D) | Dielectric constant | Viscosity (mPa s) |
|----------------------------------|--------------------|--------------------|---------------------|------------------|-----------------------|------------|---------------------|-------------------|
| 1,2-Dimethoxyethane              | -58                | 85                 | 263                 | -2               | 0.93                  | 1.71       | 7.2                 | 0.46              |
| Diethyl ether                    | -117               | 35                 | 194                 | 35               | 10.28                 | 1.3        | 4.33                | 0.224             |
| Dimethyl ether                   | -141               | -24                | 127                 | -41              | 75                    | 1.3        | 5.02                | 0.12              |
| 1,1,1,2-Tetrafluoroethane        | -103               | -26.3              | 101                 | 250              | 82                    | 2.06       | 9.7                 | 0.207             |
| Pentafluoroethane                | -103               | -48.5              | 66                  | None             | 175                   | 1.56       | 4.5                 | 0.15              |
| 1,1,1,2,3,3,3-Heptafluoropropane | -131               | -15.6              | 102                 | None             | 65.7                  | 1.46       | 2.0                 | 0.244             |
| Fluoromethane                    | -144               | -78                | 44                  | -                | 494                   | 1.85       | 9.7                 | 0.085             |

All data values are extracted from published works<sup>26,29,30,31</sup>. The vapour pressure, dipole moment, relative dielectric constant and viscosity values were obtained for solvents in a saturated liquid state at +20 °C.

moderate vapour pressure, a low melting point (down to -103 °C) and a low HOMO (highest occupied molecular orbital) energy (Table 1; Supplementary Fig. 2)<sup>35</sup>. The proposed electrolyte system is shown in Fig. 1c after combining Me<sub>2</sub>O with TFE/PFE and a salt. Owing to the strong bonding energy and low polarity of the C-F bond, TFE and PFE are expected to have a low solvation ability with Li salts and largely serve as inert agents. Nearly all Me<sub>2</sub>O solvents are coordinated to Li<sup>+</sup> and its aggregates, resulting in an enhanced oxidative stability for Me<sub>2</sub>O. Owing to the fire-extinguishing characteristics of TFE and PFE, operating the battery under harsh conditions would significantly suppress flames. By comparison, batteries using conventional flammable carbonated solvents would result in severe thermal runaway and easily cause fires. Furthermore, the moderate vapour pressure would enable a simple separation and recycling process to collect the used solvents, which is discussed in a later section.

As for selection of the salt, lithium bis(fluorosulfonyl)imide (LiFSI) and lithium bis(trifluoromethanesulfonyl)imide (LiTFSI) are considered to be appropriate salt candidates due to their lower dissociation energy than lithium hexafluorophosphate (LiPF<sub>6</sub>) and lithium tetrafluoroborate and the formation of fluorine-rich interfaces<sup>36</sup>. After performing solubility tests on LiFSI/LiTFSI-Me<sub>2</sub>O-TFE/PFE mixtures (Supplementary Figs. 3 and 4, Supplementary Note 2), 1 M LiFSI in Me<sub>2</sub>O (with a salt:Me<sub>2</sub>O molar ratio of 1:1.7) coupled with TFE (labelled as 1 M LiFSI-Me<sub>2</sub>O-TFE) and 1 M LiFSI in Me<sub>2</sub>O (salt:Me<sub>2</sub>O molar ratio 1:1.5) coupled with a TFE:PFE volume ratio of 7:1 (labelled as 1 M LiFSI-Me<sub>2</sub>O-TFE-PFE), which have a high fluorine atomic ratio, were selected for this work (Supplementary Fig. 5). A detailed comparison of the LiFSI-based and LiPF<sub>6</sub>-based LGEs is presented in the Supplementary Note 3 combined with Supplementary Figs. 6 and 7.

### Transport and safety properties

The electrolytic conductivities of the LGEs were measured and are shown in Fig. 2a. In contrast to a sharp conductivity drop observed for traditional electrolytes such as 1 M LiPF<sub>6</sub> in ethylene carbonate/ethyl methyl carbonate (EC/EMC) with a 3:7 weight ratio (labelled as 1 M LiPF<sub>6</sub>-EC-EMC) or 1 M LiFSI in 1,2-dimethoxyethane (labelled as 1 M LiFSI-DME), the LGEs 1 M LiFSI-Me<sub>2</sub>O, 1 M LiFSI-Me<sub>2</sub>O-TFE and 1 M LiFSI-Me<sub>2</sub>O-TFE-PFE exhibit a near constant conductivity >1 mS cm<sup>-1</sup> over a wide temperature range (-78 to +80 °C). The enhanced ionic conductivity at low temperature for the LGEs is attributed to the low viscosity and low melting point. Notably, conductivities measured in the 1 M LiFSI-Me<sub>2</sub>O and 1 M LiFSI-Me<sub>2</sub>O-TFE electrolytes exceed 14.1 mS cm<sup>-1</sup> and 4.5 mS cm<sup>-1</sup>, respectively, in the temperature range of -78 °C to +70 °C, which aligns with the molecular dynamics (MD) simulation results. The conductivity of the as-obtained electrolytes at low temperature compares favourably with most other electrolyte systems<sup>37,38</sup>, which

experience a severe conductivity drop at low temperature. The change in vapour pressure over a range of temperatures for different liquefied gas solvents and electrolytes is shown in Fig. 2b. In contrast to the previously proposed fluoromethane-based LGEs, the Me<sub>2</sub>O, TFE and PFE-based electrolyte and its components have a significantly lower vapour pressure. Specifically, the vapour pressure of Me<sub>2</sub>O, TFE and PFE is only 15%, 17% and 35%, respectively, of the fluoromethane vapour pressure at +20 °C. Me<sub>2</sub>O and TFE have similar vapour pressures over a wide temperature range with high critical points. We use a TFE:PFE volume ratio of 7:1 to closely follow the composition of the fire-suppressing agent FS 49 C2. This mixture has a lower operation pressure than pure PFE solvent. The resulting 1 M LiFSI-Me<sub>2</sub>O-TFE-PFE electrolyte possesses both improved safety and a wide temperature-operation window.

We then validated the fire-extinguishing effectiveness of the 1 M LiFSI-Me<sub>2</sub>O-TFE-PFE electrolyte using the fire-douse test (Supplementary Fig. 8). Tests were conducted by blowing an ignited candle with various types of gas and gas mixtures at a constant gas flow rate. Air gas is used as a reference to demonstrate that the flow rate used in the tests does not influence the flame (Fig. 2c; Supplementary Video 1). Carbon dioxide (CO<sub>2</sub>) gas shows suppression of the fire after a relatively long time of around 25 s, by gradually decreasing the local oxygen concentration (Fig. 2d; Supplementary Video 2). Meanwhile, due to the strong chemical C-F bond and faster heat adsorption, the individual TFE and PFE components effectively extinguish the fire within 1.4 s. This occurs as the agent changes from a liquid to a gas during venting in addition to the presence of C-F bonds that block the chain reactions (Supplementary Fig. 9, Supplementary Videos 3 and 4). As expected, Me<sub>2</sub>O gas demonstrates high flammability that leads to a stronger flame (Fig. 2e; Supplementary Video 5). To verify the fire-extinguishing features of the proposed 1 M LiFSI-Me<sub>2</sub>O-TFE-PFE electrolyte, the formulated electrolyte (Fig. 2f; Supplementary Video 6) itself is directly released to the flame. We observed robust fire suppression in a much shorter time than observed for pure CO<sub>2</sub> (Fig. 2d) despite the small content of Me<sub>2</sub>O present in the electrolyte (Fig. 2e). On the basis of the above results, we prove that the 1 M LiFSI-Me<sub>2</sub>O-TFE-PFE electrolyte is self-flame-extinguishing.

### Bulk structure of the electrolyte

The solvation structure of the LGEs was investigated via Raman spectroscopy using customized high-pressure cells<sup>39</sup>. To understand how the solvation structure evolves with the increase in the salt-to-ether ratio, Raman spectra at different concentrations of LiFSI in Me<sub>2</sub>O (that is, 1 M, 4 M and around 7 M (the saturated concentration)) and the formulated 1 M LiFSI-Me<sub>2</sub>O-TFE-PFE electrolyte were obtained (Fig. 3a-c). Figure 3a shows that the S-N-S bending peak is blueshifted from 730 to 748 cm<sup>-1</sup> due to the formation of FSI-(Li<sup>+</sup>)<sub>n</sub> contact-ion pairs and aggregates with

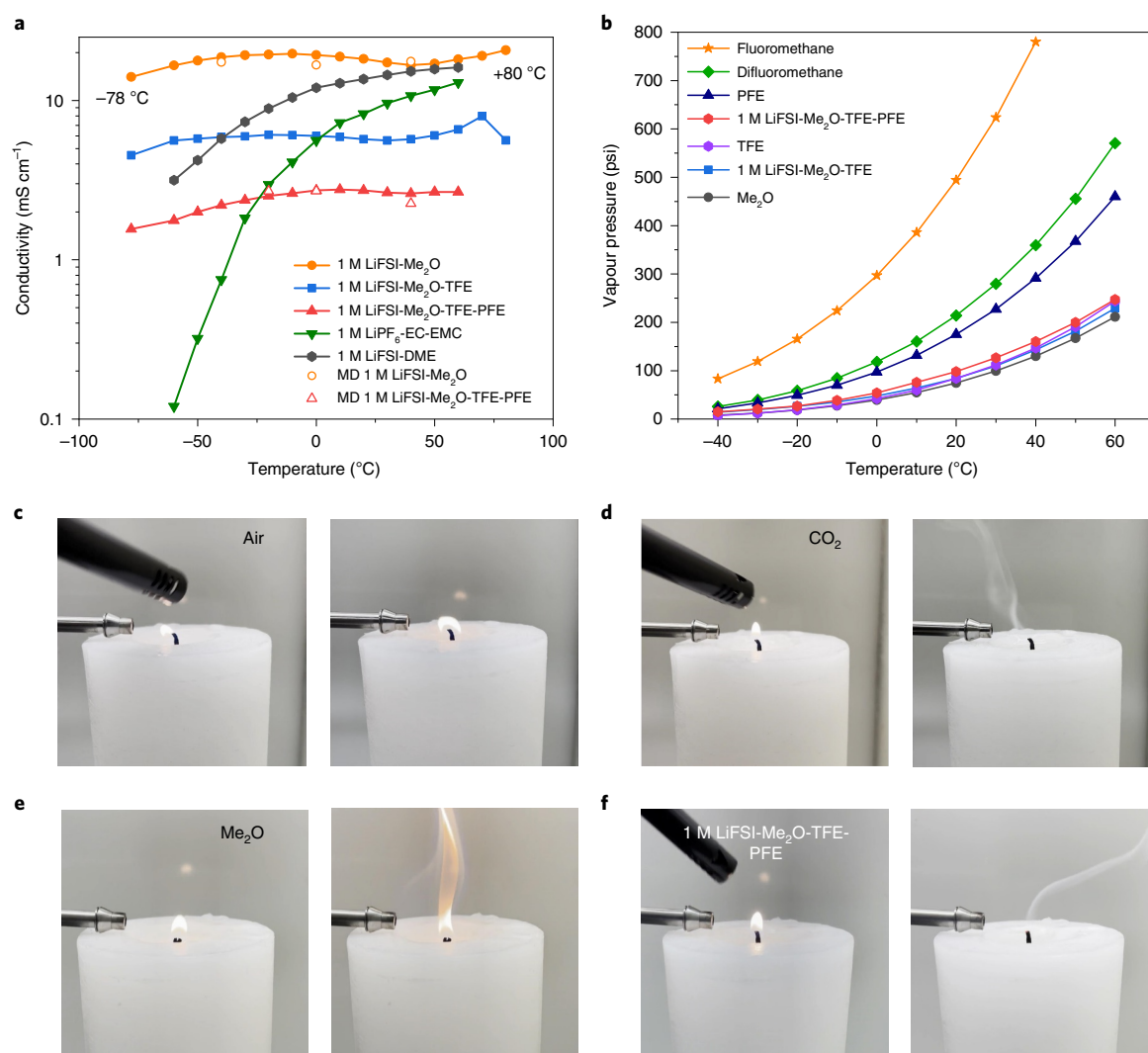


**Fig. 2 | Properties of LGEs. a**, Ionic conductivity of the LGEs over a wide temperature range. **b**, Vapour pressure of various liquefied gas solvents and electrolytes. **c–f**, Fire-douse tests with different pure gases or gas mixtures demonstrated using ignited candles with extinguishing times of air,  $+\infty$  s (**c**);  $\text{CO}_2$ ,  $25.12 \pm 0.05$  s (**d**);  $\text{Me}_2\text{O}$ , flammable, as indicated with gas off (left) and gas on (right) (**e**); and 1 M LiFSI- $\text{Me}_2\text{O}$ -TFE-PFE,  $6.53 \pm 0.03$  s (**f**).

increasing salt concentration. The saturated 7 M LiFSI in  $\text{Me}_2\text{O}$  and 1 M LiFSI- $\text{Me}_2\text{O}$ -TFE-PFE electrolytes have the same S–N–S bending peaks at  $748 \text{ cm}^{-1}$ , indicating the similarity of the salt aggregation and cluster formation, which is consistent with the similarity of the salt-to-ether ratios for these electrolytes. The peak appearing at  $721 \text{ cm}^{-1}$  for 1 M LiFSI- $\text{Me}_2\text{O}$ -TFE-PFE was assigned to the characteristic peak of the C–F<sub>3</sub> symmetric deformation, which is consistent with the pure PFE spectrum in Supplementary Fig. 10. The Raman spectrum for the TFE co-solvent is shown in Fig. 3b. A slight blueshift for the TFE molecule at  $838 \text{ cm}^{-1}$  (C–C stretching vibration) is attributed to the weak interaction between  $\text{Li}^+$  and F–CH<sub>2</sub>, which is verified by the MD simulations discussed below. For the C–O–C stretching vibration of  $\text{Me}_2\text{O}$ , a redshift for centre position from  $918$  to  $916 \text{ cm}^{-1}$  was observed, due to the increasingly solvated  $\text{Me}_2\text{O}$  in the electrolytes from the low salt concentration to the saturated salt concentration (Fig. 3c; Supplementary Fig. 11). In short, solvated FSI<sup>−</sup> and  $\text{Me}_2\text{O}$  dominate the solvation structure, which is believed to reduce the free  $\text{Me}_2\text{O}$  solvent amount leading to improvement of the oxidative stability. This facilitates the salt decomposition to form a LiF-rich SEI on the anode.

The bulk structures of the 1 M LiFSI- $\text{Me}_2\text{O}$  and 1 M LiFSI- $\text{Me}_2\text{O}$ -TFE-PFE electrolytes were examined via MD

simulations using APPLE&P force fields after validating its ability to predict the solvent- $\text{Li}^+$  binding energy obtained using quantum chemistry (QC) calculations (Supplementary Fig. 12, Supplementary Note 4). The  $\text{Li}^+$ - $\text{Me}_2\text{O}$  binding is the strongest, followed by  $\text{Li}^+$ -TFE and  $\text{Li}^+$ -PFE, indicating that TFE is more effective at salt dissociation than PFE. The MD simulations reveal a dominance of short, well-dispersed ionic aggregates in 1 M LiFSI- $\text{Me}_2\text{O}$ , although much larger aggregates were found in 1 M LiFSI- $\text{Me}_2\text{O}$ -TFE-PFE (Fig. 3d–f; Supplementary Figs. 13–15). A clear trend of an increasing extent of aggregation with increasing temperature is observed. This is consistent with increasing the  $\text{Li}^+$ -FSI<sup>−</sup> coordination and decreasing the Li–ether oxygen coordination with increasing temperature (Fig. 3g). Dilution of 1 M LiFSI- $\text{Me}_2\text{O}$  with TFE and PFE solvents decreases the fraction of ‘free’  $\text{Li}^+$  and FSI<sup>−</sup> from (12–24%) to well below 0.1%, making charge transport by free ions negligible in the 1 M LiFSI- $\text{Me}_2\text{O}$ -TFE-PFE electrolyte. Through analysis of the radial distribution functions, representative solvates and coordination numbers (Supplementary Figs. 16 and 17; Fig. 3g) reveal the strongest propensity for a  $\text{Li}^+$  to coordinate to the ether oxygen atoms of  $\text{Me}_2\text{O}$  followed by the oxygen atoms of FSI<sup>−</sup> and fluorine atoms of TFE. No coordination of  $\text{Li}^+$  to the fluorine of PFE is observed, in alignment with QC results, indicating that the

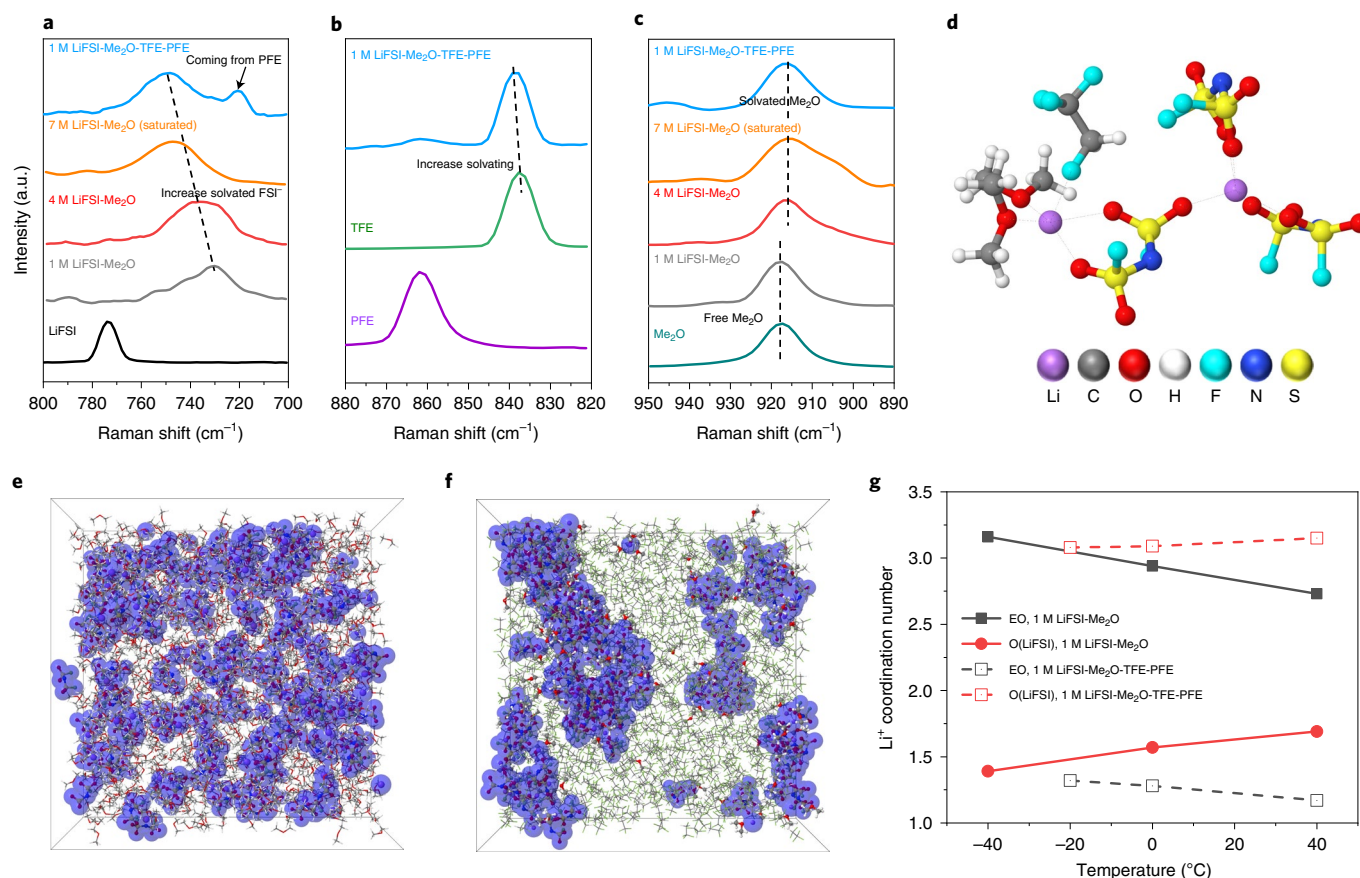


**Fig. 3 | Bulk structure and MD simulation results of the formulated electrolytes.** **a–c**, Raman spectra of electrolytes at different LiFSI concentrations in Me<sub>2</sub>O and the 1 M LiFSI-Me<sub>2</sub>O-TFE-PFE mixture at 800–700  $\text{cm}^{-1}$  (the S–N–S bending vibration of FSI<sup>-</sup>) (**a**), 880–820  $\text{cm}^{-1}$  (the C–F stretching vibration of TFE and PFE molecules) (**b**) and 950–890  $\text{cm}^{-1}$  (the C–O–C stretching vibration of Me<sub>2</sub>O) (**c**). **d–f**, Snapshots of the MD simulation cell containing the representative Li<sup>+</sup> solvates (**d**), 1 M LiFSI-Me<sub>2</sub>O (**e**) and 1 M LiFSI-Me<sub>2</sub>O-TFE-PFE (**f**) at 273 K. In **e, f**, the blue isosurfaces highlight the locations of Li<sup>+</sup> and FSI<sup>-</sup>. Colours: Li, purple; C, grey; O, red; H, white; F, cyan; N, navy blue; S, yellow. **g**, Li<sup>+</sup> coordination numbers of Li–EO bonding and Li–O (from LiFSI) bonding at different temperatures. EO, ether oxygen.

weakest binding of Li<sup>+</sup> is to the PFE solvent, in agreement with the Raman data (Fig. 3b). The most probable local Li<sup>+</sup> environments are Li<sup>+</sup>(Me<sub>2</sub>O)(FSI)<sub>2</sub> and Li<sup>+</sup>(Me<sub>2</sub>O)(FSI)<sub>3</sub>, enabling formation of the extended aggregates (Supplementary Fig. 18). Nearly all (>94%) Me<sub>2</sub>O molecules are bound to Li<sup>+</sup> in 1 M LiFSI-Me<sub>2</sub>O-TFE-PFE, resulting in improved oxidation stability due to a low fraction of ‘free’ ether solvent that is known to undergo hydrogen transfer on the LiNiO<sub>2</sub>-like cathode surfaces<sup>40</sup>.

MD simulations accurately predict the electrolyte conductivity (Fig. 2a). The conductivity decreases by a factor of six with the addition of TFE and PFE to 1 M LiFSI-Me<sub>2</sub>O. This is attributed to the decrease in ion diffusion by a factor of 2.3–2.6, and to increased ion aggregation and the elimination of free ions. The near constant conductivity with varying temperature is due to the compensation of slowed ionic motion with decreasing temperature and an increasing fraction of charge carriers due to the breakdown of the larger ionic aggregates, which results in increasing ionicity at reduced temperatures that is consistent to being closer to the ideal line in the Walden plot (Supplementary Figs. 19 and 20).

### Electrochemical performance

Li-metal soak tests were first performed to examine the compatibility of the electrolytes with Li metal (Supplementary Fig. 21, Supplementary Note 5). It was observed that the Li metal retained a clean and polished appearance after soaking in the 1 M LiFSI-Me<sub>2</sub>O,

1 M LiFSI-Me<sub>2</sub>O-TFE and 1 M LiFSI-Me<sub>2</sub>O-TFE-PFE electrolytes for 14 days. For Li-metal plating/stripping tests, the ether-based liquid electrolyte could cycle well under mild conditions (0.5 mA cm<sup>-2</sup>, 1 mAh cm<sup>-2</sup>). However, under a current density of 3 mA cm<sup>-2</sup> with a practical capacity of 3 mAh cm<sup>-2</sup>, the performance of the Li-metal anode in 1 M LiFSI-DME quickly drops after nine cycles (Fig. 4a). The cell using 1 M LiFSI-Me<sub>2</sub>O cycles with an average CE of 96.4% in the first 100 cycles, suggesting an improved Li-metal compatibility with Me<sub>2</sub>O over DME, although the CE fades in subsequent cycles. By contrast, the LGEs using 1 M LiFSI-Me<sub>2</sub>O-TFE-PFE and 1 M LiFSI-Me<sub>2</sub>O-TFE deliver first-cycle CE values of 94.8% and 96.8%, respectively. Average CE values of 98.8% and 99.0%, respectively, are achieved in the subsequent 200 cycles (Fig. 4a), demonstrating their electrochemical compatibility with Li-metal anodes and indicating the robustness of the salt-derived SEI. The 1 M LiFSI-Me<sub>2</sub>O-TFE-PFE electrolyte is further investigated over a wide temperature range, where it retains average CE values of 97.3%, 97.2%, 95.2% and 91.0% at 0, –20, –40 and –60 °C, respectively, under the same current density of 3 mA cm<sup>-2</sup> and plating capacity of 3 mAh cm<sup>-2</sup>. In comparison, 1 M LiFSI-Me<sub>2</sub>O delivers an average CE of 73.7% at –40 °C and the cell malfunctions at –60 °C with severe CE fluctuation. Although the reference 1 M LiFSI-DME liquid electrolyte cycles under mild 1 mA cm<sup>-2</sup> and 1 mAh cm<sup>-2</sup> conditions, the cell CE fades dramatically at subzero temperatures due to the solvent-dominated solvation structure and low transference number (Fig. 4b).

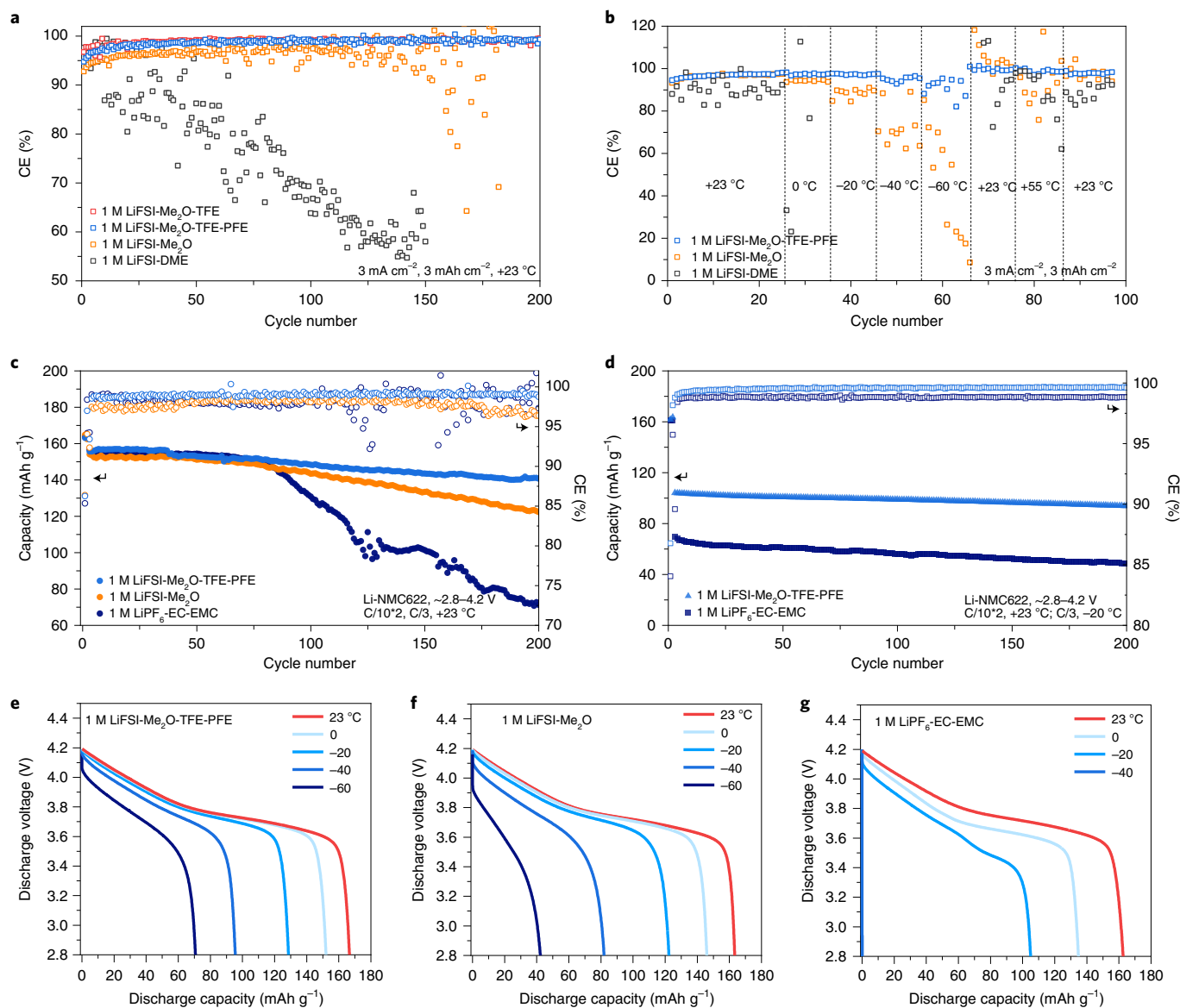


**Fig. 4 | Electrochemical performance of Li-metal anode and Li/NMC622 cells in different electrolytes. a, b**, The CE of Li-metal plating/stripping over 200 cycles in various electrolytes at +23 °C (**a**) and at different temperatures (**b**). **c, d**, Li/NMC622 long-term cycling at +23 °C (**c**) and at -20 °C (**d**). **e–g**, Li/NMC622 charging and discharging at selected temperatures for the 1 M LiFSI-Me<sub>2</sub>O-TFE-PFE electrolyte (**e**), the 1 M LiFSI-Me<sub>2</sub>O electrolyte (**f**) and the carbonate-based electrolyte (**g**). The NMC622 loading is 1.8 mAh cm<sup>-2</sup>.

Cells comprising a Li-metal anode and a LiNi<sub>0.6</sub>Mn<sub>0.2</sub>Co<sub>0.2</sub>O<sub>2</sub> cathode (NMC622) with an average loading of ~1.8 mAh cm<sup>-2</sup> were fabricated to investigate the oxidative stability of the LGE. A widely used commercial electrolyte (Gen2) consisting of 1 M LiPF<sub>6</sub> in EC/EMC with a 3:7 weight ratio was selected for the reference cell. Based on a Li/NMC622 voltage-hold test (Supplementary Fig. 22), the 1 M LiFSI-Me<sub>2</sub>O-TFE and 1 M LiFSI-Me<sub>2</sub>O-TFE-PFE electrolytes show an oxidation stability up to 4.4 V. At room temperature and a 4.2 V upper voltage, the Li/NMC622 cells in 1 M Me<sub>2</sub>O-TFE-PFE provide an average CE of >99.0% with a capacity retention of 90.4% over 200 cycles (Fig. 4c). By comparison, the carbonate-based electrolyte shows a quicker capacity fade. For the 20-μm-thick Li-metal used, this corresponds to a capacity ratio (or N/P ratio) of 2.3:1, the formulated LGE maintains a 153 mAh g<sup>-1</sup> discharge capacity over 50 cycles (Supplementary Fig. 23). At a reduced temperature (-20 °C) the 1 M LiFSI-Me<sub>2</sub>O-TFE-PFE electrolyte exhibits a high average CE of 99.6% and a capacity retention of >90.0% after 200 cycles, whereas

the carbonate-based electrolyte demonstrates a lower average CE and a reduced (70.1%) capacity retention (Fig. 4d). Furthermore, compared with Gen2, the 1 M LiFSI-Me<sub>2</sub>O-TFE-PFE electrolyte displays improved long-term cycling at +55 °C with a capacity retention of 80% after 50 cycles (Supplementary Fig. 24). Owing to the high conductivity and high transference number of 0.55 (Supplementary Fig. 25), it also shows an outstanding rate capability, with a 90% capacity retention under a C rate of 1C and no obvious capacity decay under a C rate of C/2 over 100 cycles (Supplementary Fig. 26). Besides the Li-metal anode, the formulated LGE enables reversible intercalation and de-intercalation of Li<sup>+</sup> in graphite with a CE of 99.75% over 30 cycles (Supplementary Fig. 27), indicating the compatibility of the LGE with a graphite anode.

To further evaluate the 1 M LiFSI-Me<sub>2</sub>O-TFE-PFE electrolyte performance across a wide temperature window, the Li/NMC622 cells were cycled with both carbonate- and ether-based electrolytes as references. Under the same charge and discharge rate of C/15

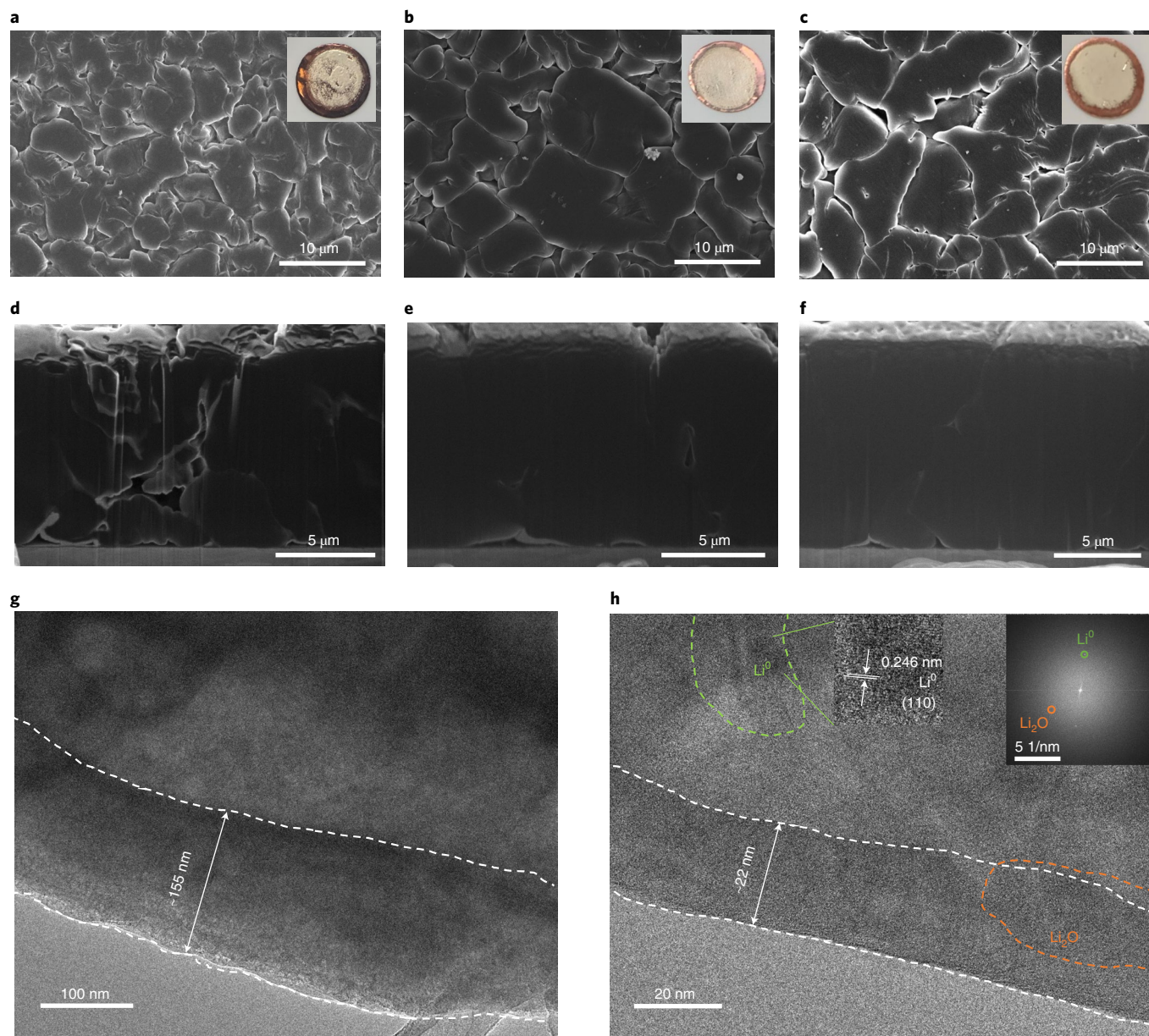


**Fig. 5 | Visualization of Li morphology and SEI.** **a–f**, Cryo-FIB/SEM images of the surface (**a–c**) and cross-section (**d–f**) of deposited Li metal after the first plating on the Cu foil using 1M LiFSI-DME (**a,d**), 1M LiFSI-Me<sub>2</sub>O (**b,e**) and 1M LiFSI-Me<sub>2</sub>O-TFE-PFE (**c,f**). Insets in **a–c**: optical images of deposited Li on the Cu foil. **g,h**, Cryo-TEM images of the deposited Li. Visualization of the SEI thickness from 1M LiFSI-DME (**g**) and 1M LiFSI-Me<sub>2</sub>O-TFE-PFE (**h**). Insets in **h**: fast Fourier transform patterns corresponding to bulk Li metal (green) and Li<sub>2</sub>O in the SEI (orange) (right); and high-resolution TEM image of crystalline Li metal (left).

and a cutoff voltage of 4.2 V, the discharge capacities are approximately the same across all three electrolytes at room temperature. At  $-60^{\circ}\text{C}$ , the 1M LiFSI-Me<sub>2</sub>O-TFE-PFE and 1M LiFSI-Me<sub>2</sub>O electrolytes demonstrate discharge capacities of 71 and 43 mAh g<sup>-1</sup>, respectively (Fig. 4e,f). By contrast, the carbonate-based electrolyte is incapable of charging and discharging at  $-40^{\circ}\text{C}$ . (Fig. 4g). On the basis of the above results, we have successfully demonstrated that the formulated LGE can maintain stable, long-term cycling at room temperature and an enhanced low-temperature performance as well as a steady rate capability. Compared with other studies that use non-flammable fluoroether solvents, the resulting LGE maintains a state-of-the-art performance with enhanced safety (Supplementary Tables 1 and 2, Supplementary Video 7), which paves the way to the development of next-generation Li-metal batteries.

### Morphology and interface chemistry characterisation

To understand the influence of the electrolytes on the surface and cross-sectional morphology of the deposited Li metal, cryogenic focused ion beam/scanning electron microscopy (cryo-FIB/SEM) was applied to mitigate potential beam damage on the Li metal<sup>41</sup>. The Li samples were plated onto a copper (Cu) foil with a 3 mAh cm<sup>-2</sup> capacity using a current density of 0.5 mA cm<sup>-2</sup>, which corresponds to an electrodeposition thickness of approximately 15 μm.

Electrolyte formulations exert a crucial influence on the electrodeposited Li metals. Here, we compare the Li-metal morphology and the thickness of the SEI formed in the LGE with the control electrolytes. Consistent with the literature<sup>42</sup>, plating in a 1M LiFSI-DME electrolyte shows a locally dense and relatively large granular Li-metal surface morphology; however, a high structural

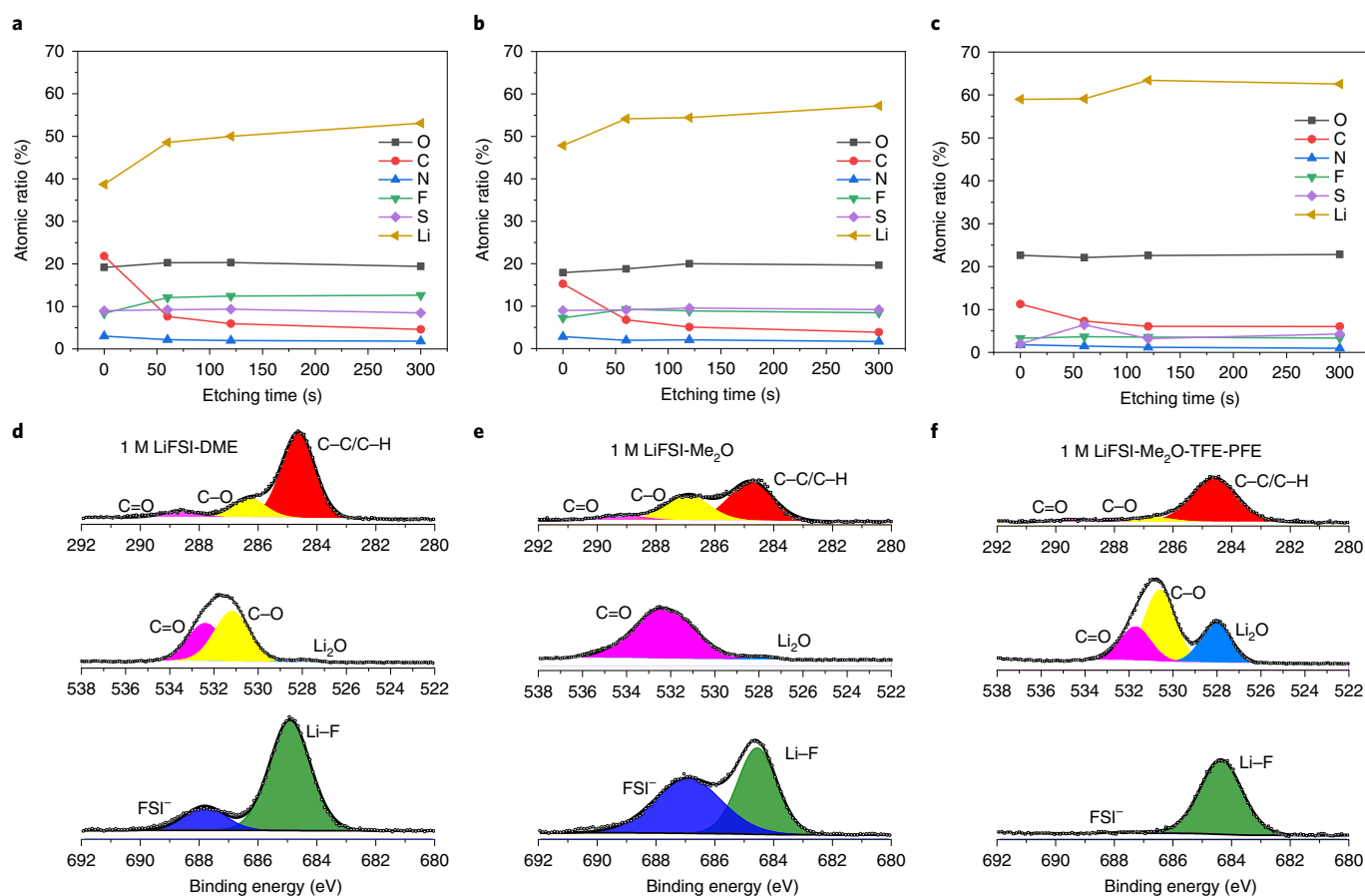


**Fig. 6 | SEI information obtained by XPS measurements with electrolytes. a–f**, Quantified atomic elemental ratios of the SEI at different sputtering times for (a–c) as well as surface spectra from cycled lithium (d–f) for 1 M LiFSI-DME (a,d), 1 M LiFSI-Me<sub>2</sub>O (b,e) and 1 M LiFSI-Me<sub>2</sub>O-TFE-PFE (c,f). For d–f, the top, middle and bottom spectra are for C 1s, O 1s and F 1s, respectively. For O 1s spectra, C=O denotes both C=O and S=O contributions.

tortuosity in the cross-section is also apparent (Fig. 5a,d). Moreover, the global distribution of the plated Li turns out to be inhomogeneous (Fig. 5a), which explains the inferior cycling stability of the DME-based electrolyte at a high current density. By contrast, both the dilute Me<sub>2</sub>O and Me<sub>2</sub>O-TFE-PFE electrolytes deliver a dense Li-metal morphology with large granule sizes and uniform global coverage (Fig. 5b,c, respectively). Although small voids are observed for the dilute Me<sub>2</sub>O electrolyte, Li metal plated from the 1 M LiFSI-Me<sub>2</sub>O-TFE-PFE electrolyte has significantly fewer voids and a dense morphology (Fig. 5e,f), indicating a lower nucleation barrier and homogeneous deposition of the Li metal. In accord with the cryo-FIB/SEM images, the Li anode after extended cycling also demonstrates a more compact morphology when cycled in 1 M LiFSI-Me<sub>2</sub>O and 1 M LiFSI-Me<sub>2</sub>O-TFE-PFE electrolytes, compared with the samples cycled in 1 M LiFSI-DME (Supplementary Fig. 28). To visualize the SEI thickness of the deposited Li in the 1 M LiFSI-DME and 1 M LiFSI-Me<sub>2</sub>O-TFE-PFE electrolytes, cryogenic transmission electron microscopy (cryo-TEM) was performed (Fig. 5g,h; Supplementary Fig. 29). Clear differences in the SEI thickness on the deposited Li are observed for the two electrolytes. The SEI formed in the 1 M LiFSI-DME electrolyte showed a thickness of ~155 nm (Fig. 5g), whereas the SEI formed in the 1 M LiFSI-Me<sub>2</sub>O-TFE-PFE electrolyte was much thinner, only 22 nm thick (Fig. 5h). Although the Li deposited in each electrolyte has a bulky structure (Supplementary Fig. 29), the ultrathick SEI on the Li deposited might deteriorate the Li||Cu cycling behaviour of the 1 M LiFSI-DME electrolyte. However, the thin and dense SEI formed on Li deposited in the 1 M LiFSI-Me<sub>2</sub>O-TFE-PFE electrolyte

is thought to give rise to the improved cycling stability. These results further illustrate that Me<sub>2</sub>O is a promising ether solvent that has electrochemical compatibility with Li metal. With an increase in the salt-to-solvent ratio, the reductive stability is further strengthened, as demonstrated in 1 M LiFSI-Me<sub>2</sub>O-TFE-PFE.

Along with the Li morphology difference, the improved cycling performance of the formulated electrolyte compared with the reference dilute-ether electrolytes can also be explained via the different chemical compositions of the respective SEI layers, as characterized using X-ray photoelectron spectroscopy (XPS) with depth profiling. The C signal, including C–C/C–H, C–O and C=O, represents organic species of the SEI. From a global survey of the C 1s atomic concentrations (Fig. 6a–c), it can be observed that the SEI formed in 1 M LiFSI-DME (Fig. 6a) has the highest carbon ratio, whereas the SEIs formed in 1 M LiFSI-Me<sub>2</sub>O (Fig. 6b) and 1 M LiFSI-Me<sub>2</sub>O-TFE-PFE (Fig. 6c) show gradually descending carbon ratios. The Li atomic concentration mostly represents the inorganic ratio inside the SEI. As shown in Fig. 6a–c, the SEI formed in 1 M LiFSI-Me<sub>2</sub>O-TFE-PFE contains the highest Li concentration at around 60%, whereas for the SEI formed in 1 M LiFSI-DME and 1 M LiFSI-Me<sub>2</sub>O it is 39% and 48%, respectively. Interestingly, with increasing etching time, the two predominating atomic concentrations of Li and O, and the secondary F, S and N atomic concentrations in the SEI formed in 1 M LiFSI-Me<sub>2</sub>O-TFE-PFE vary in a narrow range. Coupled with the observation of a homogeneously thin layer of the SEI via cryo-TEM, it shows a similar structure of the monolithic SEI reported by Cao et al.<sup>43</sup> Overall, the global survey results are consistent with the MD and Raman results, showing less

free ether solvent in the solvation structure, and further strengthening the conclusion that there is less solvent decomposition on the Li-metal surface in the 1 M LiFSI-Me<sub>2</sub>O-TFE-PFE electrolyte.

For the local survey of specific chemical information, since all electrolytes are ether-based systems, they maintain similar types of chemical composition in each individual spectrum (Fig. 6d–f; Supplementary Fig. 30). However, the differences can be seen in their relative ratios, where there are more salt-decomposed compounds such as LiF, Li<sub>2</sub>O and Li<sub>2</sub>S generated in the 1 M LiFSI-Me<sub>2</sub>O-TFE-PFE (Fig. 6f; Supplementary Fig. 30). The observation of an SEI rich in Li<sub>2</sub>O and Li<sub>2</sub>S has also been reported for some localized highly concentrated ether-based electrolytes, which might be favourable SEI components for the Li-metal anode<sup>43–45</sup>. For the two reference electrolytes, there are clearly indicated more organic C–O, S=O, and C=O compounds (Fig. 6d,e; Supplementary Fig. 30). The appearance of the organic compounds suggests that there is more decomposition of the DME (Fig. 6d) or Me<sub>2</sub>O solvents (Fig. 6e), leading to the relatively poor electrochemical stability with Li metal.

### Recyclability of liquefied gas solvent

Battery recycling is crucial for reducing costs and removing the potential risks that battery components pose to the environment. To better understand the bottleneck of the battery-recycling process, a closed loop for Li-metal battery recycling is illustrated in Fig. 7a. Even with lean electrolyte conditions, the electrolyte still occupies a large ratio by weight (24%)<sup>23</sup> in Li/NMC pouch cells. The electrolyte ratio would be even higher for more porous electrodes, such as sulfur. However, the electrolyte is not recovered but is simply disposed of during the electrolyte-handling process or it is not mentioned in most published studies<sup>46,47</sup>. In view of the porous, high surface area of the electrodes and the high viscosity of the electrolyte, for efficient collection of the spent electrolytes the primary challenge is to separate the electrolyte from the electrodes<sup>48</sup>. Conventionally, supercritical CO<sub>2</sub> is employed for electrolyte extraction from both separators and electrode materials owing to its enhanced dissolution characteristics. In addition, the electrolyte salt and solvents can all be recovered when the extractant CO<sub>2</sub> is supplemented with some functional additives (for example, acetonitrile and propylene carbonate)<sup>49</sup>. However, considering the intrinsic high-pressure nature of supercritical CO<sub>2</sub>, the cost of this technique limits its wide application. By comparison, owing to the low viscosity and low boiling point of LGE systems, the ease of evaporation controlled via temperature changes would not require a complicated separation process. Furthermore, the commercialization of LGE technology on a large scale will require the recycling of hydrofluorocarbon gases, otherwise the stable C–F bonds from these gases would cause a noticeable global-warming effect (Supplementary Fig. 31).

To overcome the above issues, a practical LGE recycling process is proposed using the relationship between vapour pressure ( $P_{\text{vapour}}$ ) and temperature in liquefied gas solvents (Fig. 7b). If a temperature difference is generated between two connected containers with a liquefied solvent inside, the solvent will transfer and liquefy in the low-temperature container. This solvent transfer is driven by the pressure gradient generated from the temperature difference. The proposed method is a simple approach for the collection and reuse of the liquefied gas solvent. Tests using window cells were performed first as a control to directly observe the solvent transport (Fig. 7c). A window cell with 1 M LiFSI-Me<sub>2</sub>O-TFE was placed in a temperature chamber at a higher temperature (+40 °C,  $P_{\text{vapour}} = 143$  psi), and was connected to a second window cell with the same amount of LiFSI in the chamber but at a lower temperature (–40 °C,  $P_{\text{vapour}} = 13.9$  psi). Driven by the large pressure difference, most of the solvent in the high-temperature cell was transferred and liquefied in the lower-temperature cell. This resulted in a well-mixed, new 1 M LiFSI-Me<sub>2</sub>O-TFE-PFE electrolyte, demonstrating

the capability of recycling the LGE. Using the same process, the solvent of 1 M LiFSI-Me<sub>2</sub>O-TFE-PFE in a cycled Li/NMC coin cell was successfully transferred to a newly assembled Li/NMC cell without adding any extra solvent. Notably, the performance of the recycled cell showed nearly identical capacity and efficiency profiles and a similar voltage profile compared with the original cell (Fig. 7d). These results demonstrate the effectiveness of this simple solvent-recycling process, which can be easily integrated to the standard assembly process of liquefied gas cells (Supplementary Note 6, Supplementary Fig. 32). With further optimizations, this is a promising process for practical LGE recycling. The successful recycling of Me<sub>2</sub>O and hydrofluorocarbon co-solvents in the electrolyte solutions not only creates new applications for by-products synthesized from the conventional petroleum industry but also provides the opportunity for sustainable energy.

### Conclusion

We rationally designed an LGE by adding the simplest (liquefied) ether to a non-flammable low-solvating hydrofluorocarbon mixture. The resulting LGE is not only non-flammable but has a fire-extinguishing feature. It delivers a high performance over a wide temperature range (–78 to +80 °C) and enables a stable Li-metal and Li/NMC cycling with high CE values. A practical electrolyte-recycling process was demonstrated using the vapour pressure–temperature relationship of liquefied gas solvents. The electrochemical, safety and recycling properties of the LGE are derived directly from their physical and chemical properties. This study provides an insight into designing multifunctional electrolytes and presents an encouraging path towards safer batteries with a wide operation-temperature range and a feasible recycling process.

### Methods

**Materials.** Me<sub>2</sub>O (99%) was obtained from Sigma-Aldrich. TFE (99%), PFE (99%) and 1,1,1,2,3,3,3-heptafluoropropane (98%) were purchased from SynQuest Labs. The salts LiFSI (99.9%) and LiTFSI (99.9%) were purchased from BASF. The Gen2 electrolyte 1 M LiPF<sub>6</sub> in EC/EMC 3:7 was obtained from BASF. DME (99.5%) was purchased from Sigma-Aldrich and stored with molecular sieves. The NMC622 (A-C023) was supplied by Argonne National Laboratory; it was casted on aluminium foil, and was heated and rolled before use. Lithium foils (20 μm thick) were supplied from Applied Materials.

**Electrochemical measurements.** The conductivity of the electrolytes was measured using a custom-fabricated high-pressure stainless-steel (SS) cell setup, with polished SS (316L grade) as the electrodes. Calibration of the cell constant was performed using OAKTON standard conductivity solutions (0.447–80 mS cm<sup>–1</sup>).

The transference number of Li<sup>+</sup> in the electrolyte was measured using a potentiostatic polarization method with an applied voltage of 5 mV. The cell setup consisted of two Li-metal foils sandwiched between 500-μm-thick glass-fibre separators. Electrochemical impedance spectroscopy data were collected using a Biologic SAS (SP-200) system, and ZView software was used to fit the spectra.

Customized high-pressure SS (316L) cells were used for battery cycling using an Arbin battery test station cycler (BT2043). Li metal (1 mm thickness, 3/8 inch diameter, FMC Lithium; counter electrode) and polished SS (316L; working electrode) with a single 25 μm porous polypropylene separator (Celgard 2075) were used for all the electrochemical tests. Flooded electrolytes of more than 50 g Ah<sup>–1</sup> were added to all cells. The initial stacking pressure was around 200–400 kPa. The testing temperature was on average 23 °C without any specific control.

For the plating and stripping experiments of Li/SS, a discharge current density of 0.5 mA cm<sup>–2</sup> was applied until 0 V versus Li, and the voltage was then held for 5 h to form a stable SEI on the current collector. After SEI formation, plating was started and followed by stripping until a 1 V versus Li cutoff voltage. The CE of the cycling was calculated as the Li stripping capacity divided by the Li plating capacity during each cycle. For testing at different temperatures, the cells were soaked at the testing temperature, using a temperature chamber (Espec), for several hours before cycling. Two activation cycles using the C/10 rate at room temperature were performed for the Li/NMC cells, and they were then cycled at selected rates and temperatures.

**Material characterization.** The pressure measurements of different pure gases or formulated LGE were performed using a Honeywell FP5000 pressure sensor from –40 to +60 °C.

Li-metal soak tests were performed using a custom-built SS cell withstanding up to 2,000 psi. All Li-metal samples were soaked in the corresponding electrolytes

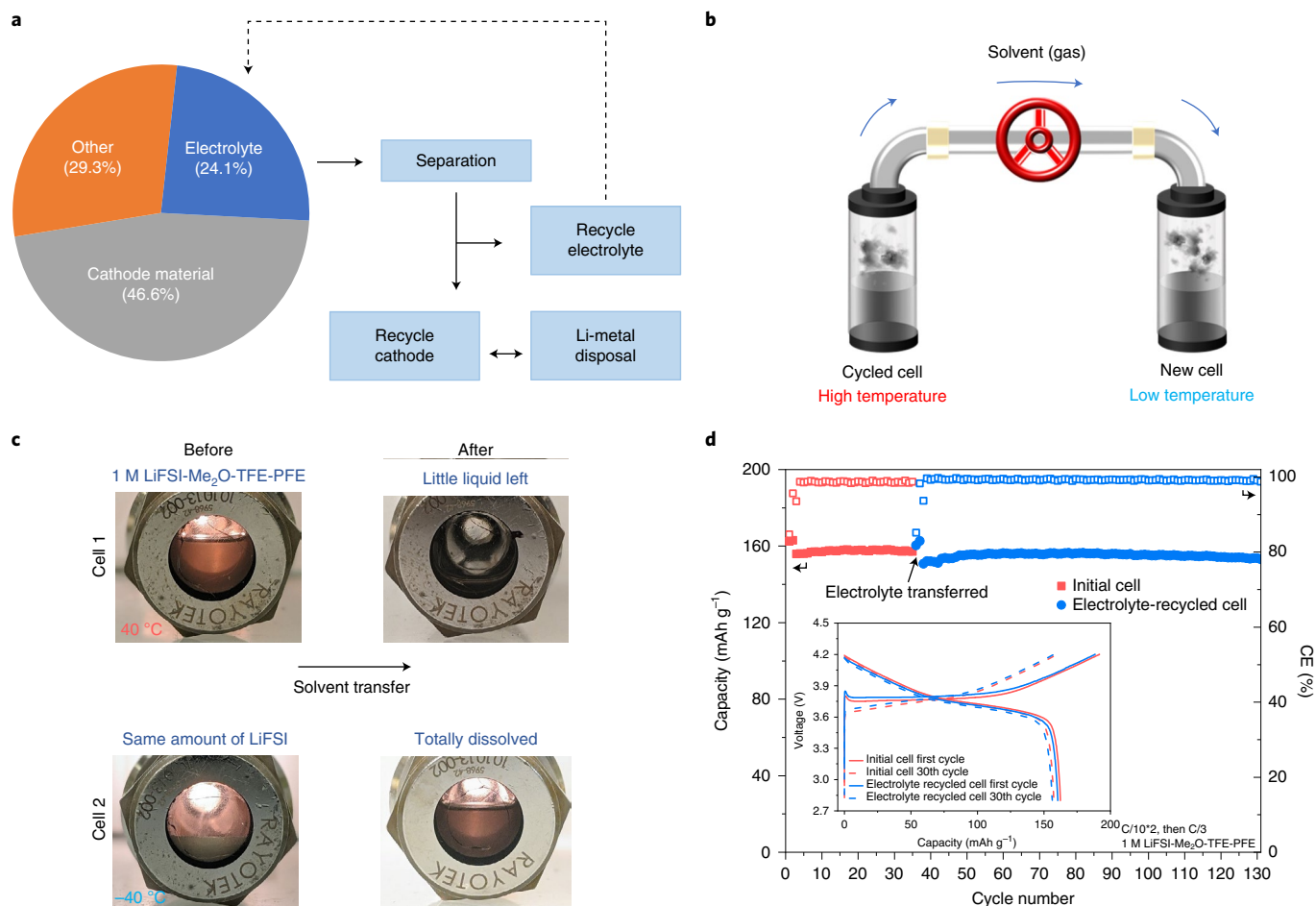


**Fig. 7 | Recycling concept and demonstration of LGEs.** **a**, Schematic of the potential closed-loop, direct recycling process of liquid-based electrolytes. **b**, Schematic of the practical process of liquefied gas solvent collection and recycling. **c**, Demonstration of solvent transfer between two separate window cells. Initially, cell with electrolyte is soaked at +40 °C (top) and the other cell is soaked at -40 °C preloaded with LiFSI salt (bottom). **d**, Comparison of the electrochemical performance of a Li/NMC622 system for the initial cell and the cell using recycled solvents. Inset: the charge-discharge curves of the cells at specific cycles.

for periods of half a month. The optical images were taken after disassembling the soak cells.

Fire-extinguishing experiments were conducted using a fume hood with the following fixed parameters: gas flow at 150 sccm (standard cubic centimetres per minute), relative height and distance of safety cell and candle, and an open system within the fume hood (Supplementary Fig. 8). The experiments are set up with a safety cell connected to a mass flow controller and an SS tube with a valve for precise control of the gas flow. The cell serves to isolate the gas tanks from the ignited candle for a safe operating environment. A constant gas flow is maintained by the mass flow controller while the relative height and distance between the cell and candle are fixed using two utility clamps. Subsequently, the different gas types were used with this experimental setup to demonstrate their fire-extinguishing efficacy.

A Renishaw inVia confocal Raman microscope was used for obtaining the Raman spectra of the LGEs, with a green laser of excitation wavelength 532 nm. Silicon (520 nm) was used to calibrate all the spectra, with subsequent analysis performed using WiRE 3.4 software developed by Renishaw Ltd.

The surface and cross-sectional morphology of the deposited Li was observed using an FEI Scios Dual Beam FIB scanning electron microscope. The operating voltage and emission current of the electron beam were 5 kV and 0.1 nA, respectively. A gallium-ion beam source was used to mill the sample. The operating voltage of the ion-beam source was 30 kV. Different emission currents of the ion beam were chosen for different purposes, that is, 5 nA for pattern milling, 10 pA for imaging by the ion beam and 0.3 nA for cross-section cleaning. During ion-beam milling, the stage temperature was maintained at -175 °C to prevent beam damage on the Li-metal sample.

The cryo-TEM samples were prepared by electrochemically depositing Li onto TEM grids in the Li||Cu cells. The cells were tested at a current density of

2 mA cm<sup>-2</sup> to plate Li for 5 min. After Li deposition, the TEM sample grids were rinsed lightly with DME to remove trace Li salts in an argon-filled glovebox. Once they have been dried under vacuum, the sample grids were sealed in airtight bags before being transferred to the TEM facility. The sample grids were mounted onto a TEM cryo-holder (Gatan) via a cryotransfer station. In short, the whole TEM sample preparation-and-transfer process prevented any air exposure to the Li metal at room temperature. TEM characterization was carried out using a JEM-2100F instrument at 200 kV. High-resolution TEM images were obtained at a magnification of ×300,000 using a Gatan OneView Camera (full 4k×4k resolution) when the temperature of the samples reached about 100 K. Fast Fourier transform patterns were analysed using Digital Micrograph software.

The XPS samples were prepared via electrochemical cycling in the Li||Cu cells. The cells were tested at a current density of 1 mA cm<sup>-2</sup> and a capacity of 1 mAh cm<sup>-2</sup> over 50 cycles. Then, the deposited Li samples on the Cu side were lightly washed with DME solvent to remove trace Li salts in an argon-filled glovebox and dried inside the glovebox antechamber. To avoid moisture and air exposure, sealed samples were transferred to the XPS chamber directly using a nitrogen-filled glovebox via vacuum transfer. Then, the experiments were performed using a Kratos AXIS Supra DLD XPS instrument with monochromatized Al K $\alpha$  radiation ( $\lambda = 0.83$  nm and  $h\nu = 1,486.7$  eV) under a base pressure of <math>10^{-8}</math> Pa (ref. 28). CasaXPS software was used to perform the XPS analysis, for which all spectra were calibrated with hydrocarbon C 1s (284.6 eV). The etching condition was set as an Al<sub>2500</sub><sup>+</sup> cluster at 5 keV. The etching times were 60 s, 120 s and 300 s.

**Simulations.** The HOMO and LUMO (lowest unoccupied molecular orbital) energies were obtained via density functional theory (DFT) calculations performed using Q-Chem 5.2 software. Single molecules were assembled and subjected to

gas-phase DFT geometry optimization using the 6-31+G\* basis set of Pople and co-workers<sup>50</sup> and the B3LYP<sup>51</sup> functional, which gave a well-balanced level of theory whilst providing a reasonable compromise between speed and accuracy. To obtain the final orbital energies, single-point energy calculations were performed on the molecules post-optimization at the B3LYP/6-311++G\*\* level of theory.

MD simulations were performed using a revised many-body polarizable APPLE&P (Atomistic Polarizable Potential for Liquids, Electrolytes & Polymers) force field that utilizes atomic-induced dipoles to describe the polarization<sup>52,53</sup>. A complete set of force-field parameters, connectivity files and the MD simulation code is provided as an archive file in the Supplementary Information. We evaluated the ability of the force field to describe the gas-phase binding energies of the Li<sup>+</sup> cation to the Me<sub>2</sub>O, TFE and PFE solvents obtained from QC calculations as shown in Supplementary Fig. 12. The basis set superposition error (or BSSE) correction was applied to all Møller–Plesset perturbation theory to the second order (MP2) using the aug-cc-pvTz (abbreviated as Tz) basis set. Binding energies from molecular mechanics using the force field were in good agreement with the MP2/Tz and composite G4MP2 results, describing accurately the order of the Li–solvent binding.

The MD simulation cells of 1 M LiFSI–Me<sub>2</sub>O contained 100 LiFSI and 1,292 Me<sub>2</sub>O molecules, whereas the 1 M LiFSI–Me<sub>2</sub>O–TFE–PFE simulation cells contained 100 LiFSI, 136 Me<sub>2</sub>O, 946 TFE and 115 PFE molecules. The simulation times, densities, transport and structural properties are summarized in Supplementary Tables 3 and 4. Multiple replicas were simulated at different temperatures to estimate the error bars. Simulations were performed in a constant volume–temperature (NVT) ensemble using a Nosé–Hoover thermostat. Multiple timestep integration was used with a timestep of 0.5 fs for bonded interactions and 1.5 fs for all non-bonded interactions within a truncation distance of 8.0 Å, and an outer timestep of 3.0 fs for all non-bonded interactions between 8.0 Å and the non-bonded truncation distance of 14 Å. Because the heterogeneous structure of the electrolyte with large ionic aggregates was surrounded by the relatively low-density solvent, a number of additional simulations were performed with a shorter non-bonded truncation distance of 12 Å instead of 14 Å to ensure that the predicted properties were not influenced by the choice of truncation distance, as shown Supplementary Table 4. The Ewald summation method was used for the electrostatic interactions between permanent charges and permanent charges or induced dipole moments with  $k=8^3$  vectors. The reciprocal part of the Ewald summation method was calculated every 3.0 fs. Induced dipoles were found using self-consistent iteration with the convergence criteria of  $10^{-9}$  (electron charge \* Å)<sup>2</sup>.

In spite of the fast solvent and ion diffusion, the residence times of Li<sup>+</sup> near the Me<sub>2</sub>O solvent and FSI<sup>−</sup> were rather long, at 7 ns and 10 ns, respectively, at 0 °C for the 1 M LiFSI–Me<sub>2</sub>O–TFE–PFE electrolyte, compared with 0.5 ns and 2.7 ns for 1 M LiFSI–Me<sub>2</sub>O at 0 °C. The increased residence time for Li–Me<sub>2</sub>O in 1 M LiFSI–Me<sub>2</sub>O–TFE–PFE compared with the 1 M LiFSI–Me<sub>2</sub>O electrolyte is attributed to the formation of much longer aggregates and the lack of ‘free’ Me<sub>2</sub>O that is needed for efficient exchange of the ‘complexed’ Me<sub>2</sub>O with the ‘free’ Me<sub>2</sub>O. The LiFSI residence time is the slowest relaxation timescale in both electrolytes and requires the MD simulations to be longer than the relaxation time by a factor of between five and ten to properly average the Li<sup>+</sup> environments and obtain an accurate estimate for the degree of ion dynamic correlation that is often called ionicity, as shown in Supplementary Fig. 19.

## Data availability

All the data generated in this study are included in the Article and its Supplementary Information. Source data are provided with this paper.

## Code availability

The MD simulation code is available in Supplementary Data 1.

Received: 23 November 2021; Accepted: 6 May 2022;

Published online: 16 June 2022

## References

- Hesse, H. C., Schimpe, M., Kucevic, D. & Jossen, A. Lithium-ion battery storage for the grid—a review of stationary battery storage system design tailored for applications in modern power grids. *Energies* **10**, 2107 (2017).
- Chen, S. et al. High-efficiency lithium metal batteries with fire-retardant electrolytes. *Joule* **2**, 1548–1558 (2018).
- Fan, X. et al. Non-flammable electrolyte enables Li-metal batteries with aggressive cathode chemistries. *Nat. Nanotechnol.* **13**, 715–722 (2018).
- Hobold, G. M. et al. Moving beyond 99.9% Coulombic efficiency for lithium anodes in liquid electrolytes. *Nat. Energy* **6**, 951–960 (2021).
- Liu, Y. et al. Making Li-metal electrodes rechargeable by controlling the dendrite growth direction. *Nat. Energy* **2**, 17083 (2017).
- Fang, C. et al. Quantifying inactive lithium in lithium metal batteries. *Nature* **572**, 511–515 (2019).
- Wang, J. et al. Improving cyclability of Li metal batteries at elevated temperatures and its origin revealed by cryo-electron microscopy. *Nat. Energy* **4**, 664–670 (2019).
- Hess, S., Wohlfahrt-Mehrens, M. & Wachtler, M. Flammability of Li-ion battery electrolytes: flash point and self-extinguishing time measurements. *J. Electrochem. Soc.* **162**, A3084–A3097 (2015).
- Xu, K., Zhang, S., Allen, J. L. & Jow, T. R. Evaluation of fluorinated alkyl phosphates as flame retardants in electrolytes for Li-ion batteries: II. Performance in cell. *J. Electrochem. Soc.* **150**, A170 (2003).
- Xu, P. et al. Efficient direct recycling of lithium-ion battery cathodes by targeted healing. *Joule* **4**, 2609–2626 (2020).
- Xu, P., Tan, D. H. S. & Chen, Z. Emerging trends in sustainable battery chemistries. *Trends Chem.* **3**, 620–630 (2021).
- Tan, D. H., Banerjee, A., Chen, Z. & Meng, Y. S. From nanoscale interface characterization to sustainable energy storage using all-solid-state batteries. *Nat. Nanotechnol.* **15**, 170–180 (2020).
- Sun, H. et al. High-safety and high-energy-density lithium metal batteries in a novel ionic-liquid electrolyte. *Adv. Mater.* **32**, 2001741 (2020).
- Banerjee, A., Wang, X., Fang, C., Wu, E. A. & Meng, Y. S. Interfaces and interphases in all-solid-state batteries with inorganic solid electrolytes. *Chem. Rev.* **120**, 6878–6933 (2020).
- Wu, L. et al. A new phosphate-based nonflammable electrolyte solvent for Li-ion batteries. *J. Power Sources* **188**, 570–573 (2009).
- Zeng, Z. et al. Safer lithium ion batteries based on nonflammable electrolyte. *J. Power Sources* **279**, 6–12 (2015).
- Shiga, T., Kato, Y., Kondo, H. & Okuda, C.-A. Self-extinguishing electrolytes using fluorinated alkyl phosphates for lithium batteries. *J. Mater. Chem. A* **5**, 5156–5162 (2017).
- Ota, H., Kominato, A., Chun, W.-J., Yasukawa, E. & Kasuya, S. Effect of cyclic phosphate additive in non-flammable electrolyte. *J. Power Sources* **119–121**, 393–398 (2003).
- Wang, J. et al. Fire-extinguishing organic electrolytes for safe batteries. *Nat. Energy* **3**, 22–29 (2018).
- Chen, S. et al. High-voltage lithium-metal batteries enabled by localized high-concentration electrolytes. *Adv. Mater.* **30**, 1706102 (2018).
- Ren, X. et al. Localized high-concentration sulfone electrolytes for high-efficiency lithium-metal batteries. *Chem* **4**, 1877–1892 (2018).
- Cao, X. et al. Nonflammable electrolytes for lithium ion batteries enabled by ultraconformal passivation interphases. *ACS Energy Lett.* **4**, 2529–2534 (2019).
- Niu, C. et al. High-energy lithium metal pouch cells with limited anode swelling and long stable cycles. *Nat. Energy* **4**, 551–559 (2019).
- Fan, X. et al. All-temperature batteries enabled by fluorinated electrolytes with non-polar solvents. *Nat. Energy* **4**, 882–890 (2019).
- Wang, Q., Mao, B., Stolarov, S. I. & Sun, J. A review of lithium ion battery failure mechanisms and fire prevention strategies. *Prog. Energy Combust. Sci.* **73**, 95–131 (2019).
- Rustomji, C. S. et al. Liquefied gas electrolytes for electrochemical energy storage devices. *Science*, <https://doi.org/10.1126/science.aal4263> (2017).
- Yang, Y. et al. High-efficiency lithium-metal anode enabled by liquefied gas electrolytes. *Joule* **3**, 1986–2000 (2019).
- Yang, Y. et al. Liquefied gas electrolytes for wide-temperature lithium metal batteries. *Energy Environ. Sci.* **13**, 2209–2219 (2020).
- Wu, J., Liu, Z., Bi, S. & Meng, X. Viscosity of saturated liquid dimethyl ether from (227 to 343) K. *J. Chem. Eng. Data* **48**, 426–429 (2003).
- Wu, J. & Yin, J. Vapor pressure measurements of dimethyl ether from (213 to 393) K. *J. Chem. Eng. Data* **53**, 2247–2249 (2008).
- Prince, J. C. & Williams, F. A. A short reaction mechanism for the combustion of dimethyl-ether. *Combust. Flame* **162**, 3589–3595 (2015).
- Westmoreland, P. R., Burgess, D. R. F., Zachariah, M. R. & Tsang, W. Fluoromethane chemistry and its role in flame suppression. *Symp. (Int.) Combust.* **25**, 1505–1511 (1994).
- Holcomb, C. D., Magee, J. W., Scott, J. L., Outcalt, S. L. & Haynes, W. M. *Selected Thermodynamic Properties for Mixtures of R-32 (Difluoromethane), R-125 (Pentafluoroethane), R-134A (1,1,1,2-Tetrafluoroethane), R-143A (1,1,1-Trifluoroethane), R-41 (Fluoromethane), R-290 (Propane), and R-744 (Carbon Dioxide)* (NIST, 1997).
- Sun, L.-Q., Zhu, M.-S., Han, L.-Z. & Lin, Z.-Z. Viscosity of difluoromethane and pentafluoroethane along the saturation line. *J. Chem. Eng. Data* **41**, 292–296 (1996).
- Wang, T., Hu, Y.-j., Zhang, P. & Pan, R.-m. Study on thermal decomposition properties and its decomposition mechanism of pentafluoroethane (HFC-125) fire extinguishing agent. *J. Fluor. Chem.* **190**, 48–55 (2016).
- von Aspern, N., Rösenthaller, G.-V., Winter, M. & Cekic-Laskovic, I. Fluorine and lithium: ideal partners for high-performance rechargeable battery electrolytes. *Angew. Chem. Int. Ed.* <https://doi.org/10.1002/anie.201901381> (2019).
- Holoubek, J. et al. Tailoring electrolyte solvation for Li metal batteries cycled at ultra-low temperature. *Nat. Energy* **6**, 303–313 (2021).
- Cai, G. et al. Sub-nanometer confinement enables facile condensation of gas electrolyte for low-temperature batteries. *Nat. Commun.* **12**, 3395 (2021).

39. Davies, D. M. et al. A safer, wide-temperature liquefied gas electrolyte based on difluoromethane. *J. Power Sources* **493**, 229668 (2021).
40. Dong, X. et al. High-energy rechargeable metallic lithium battery at  $-70^{\circ}\text{C}$  enabled by a cosolvent electrolyte. *Angew. Chem. Int. Ed.* **58**, 5623–5627 (2019).
41. Wang, X., Li, Y. & Meng, Y. S. Cryogenic electron microscopy for characterizing and diagnosing batteries. *Joule* **2**, 2225–2234 (2018).
42. Qian, J. et al. High rate and stable cycling of lithium metal anode. *Nat. Commun.* **6**, 6362 (2015).
43. Cao, X. et al. Monolithic solid–electrolyte interphases formed in fluorinated orthoformate-based electrolytes minimize Li depletion and pulverization. *Nat. Energy* **4**, 796–805 (2019).
44. Chen, H. et al. Uniform high ionic conducting lithium sulfide protection layer for stable lithium metal anode. *Adv. Energy Mater.* **9**, 1900858 (2019).
45. Kim, M. S. et al. Suspension electrolyte with modified  $\text{Li}^+$  solvation environment for lithium metal batteries. *Nat. Mater.* **21**, 445–454 (2022).
46. Lain, M. J. Recycling of lithium ion cells and batteries. *J. Power Sources* **97**, 736–738 (2001).
47. Georgi-Maschler, T., Friedrich, B., Weyhe, R., Heegn, H. & Rutz, M. Development of a recycling process for Li-ion batteries. *J. Power Sources* **207**, 173–182 (2012).
48. Sloop, S. et al. A direct recycling case study from a lithium-ion battery recall. *Sustain. Mater. Technol.* **25**, e00152 (2020).
49. Nowak, S. & Winter, M. The role of sub- and supercritical  $\text{CO}_2$  as ‘processing solvent’ for the recycling and sample preparation of lithium ion battery electrolytes. *Molecules* **22**, 403 (2017).
50. Hehre, W. Radom, L., Pople, J. & v. R. Schleyer, P. *Ab Initio Molecular Orbital Theory* (Wiley, 1986).
51. Laming, G. J., Termath, V. & Handy, N. C. A general purpose exchange-correlation energy functional. *J. Chem. Phys.* **99**, 8765–8773 (1993).
52. Borodin, O. Polarizable force field development and molecular dynamics simulations of ionic liquids. *J. Phys. Chem. B* **113**, 11463–11478 (2009).
53. Suo, L. et al. ‘Water-in-salt’ electrolyte enables high-voltage aqueous lithium-ion chemistries. *Science* **350**, 938–943 (2015).

## Acknowledgements

Y. Yin and Y.S.M. thank C. Rustomji from South 8 Technologies for the fruitful discussions. The experimental part of the work performed at UCSD was supported by Sustainable Power and Energy Center (SPEC) and Zable endowed chair fund for energy technologies. The molecular modelling performed at ARL was supported by the Assistant Secretary for Energy Efficiency and Renewable Energy, Vehicle Technology Office of the U.S. DOE through Applied Battery Research for Transportation (ABRT) program via interagency agreement 89243319SEE000004 supporting contract No. DE-SC0012704. The cryo-FIB and SEM were developed and performed in part at the

San Diego Nanotechnology Infrastructure (SDNI) of UCSD, a member of the National Nanotechnology Coordinated Infrastructure, which is supported by the National Science Foundation (Grant ECCS-1542148). Y. Yin thanks I. C. Tran for their help regarding XPS experiments performed at the University of California Irvine Materials Research Institute (IMRI) using instrumentation funded in part by the National Science Foundation Major Research Instrumentation Program (grant CHE-1338173). The authors acknowledge the use of Raman instrumentation supported by NSF through the UC San Diego Materials Research Science and Engineering Center (UCSD MRSEC), grant number DMR-2011924. We appreciate the supply of  $20\ \mu\text{m}$  lithium foils from Applied Materials.

## Author contributions

Y. Yin, Y. Yang and Y.S.M. formulated the electrolytes and designed the experiments. Y.S.M., M.M. and Y. Yang conceived the recycling process. Y. Yin and Y. Yang designed and performed the demonstration experiments. Y.S.M. and Y. Yang supervised the project. Y. Yin and Y. Yang conducted the electrochemical experiments. Y. Yin, D.C. and A.L. performed the flame-extinguishing tests with some guidance from Z.C. Raman spectroscopy was performed by Y. Yin based on cells designed by D.M.D. The force field was developed by O.B., who also carried out the MD simulations. D.C. performed the cryo-FIB. W.L. and Y. Yin performed the XPS characterization and analysis. J.H. performed the DFT calculations. G.R. and A.L. helped with control experiments. B.L. performed the cryo-TEM. Y. Yin, Y. Yang, D.C., O.B. and M.M. prepared the manuscript with input from all co-authors. All authors have given approval to the final version of the manuscript.

## Competing interests

Y. Yin, Y. Yang, M.M. and Y.S.M. declare that this work has been filed as US Provisional Patent Application No. 63/268,910. The remaining authors declare no competing interests. Y.S.M. is a member of the scientific advisory board for South 8 Technologies.

## Additional information

**Supplementary information** The online version contains supplementary material available at <https://doi.org/10.1038/s41560-022-01051-4>.

**Correspondence and requests for materials** should be addressed to Yangyuchen Yang, Oleg Borodin or Y. Shirley Meng.

**Peer review information** *Nature Energy* thanks Jinkui Feng, Jang-Kyo Kim and Matthew McDowell for their contribution to the peer review of this work.

**Reprints and permissions information** is available at [www.nature.com/reprints](http://www.nature.com/reprints).

**Publisher's note** Springer Nature remains neutral with regard to jurisdictional claims in published maps and institutional affiliations.

© The Author(s), under exclusive licence to Springer Nature Limited 2022